Magnetoelectric Assisted 180° Magnetization Switching for Electric Field Addressable Writing in Magnetoresistive Random-Access Memory

Zhiguang Wang,[†,*] Yue Zhang,[†] Yaojin Wang,[†] Yanxi Li,[†] Haosu Luo,[‡] Jiefang Li,[†] and Dwight Viehland[†]

[†]Department of Materials Science and Engineering, Virginia Tech, Blacksburg, Virginia 24061, United States and [‡]State Key Laboratory of High Performance Ceramics and Superfine Microstructure, Shanghai Institute of Ceramics, Chinese Academy of Sciences, Shanghai 201800, China

ABSTRACT Magnetization-based memories, *e.g.*, hard drive and magnetoresistive random-access memory (MRAM), use bistable magnetic domains in patterned nanomagnets for information recording. Electric field (*E*) tunable magnetic anisotropy can lower the energy barrier between two distinct magnetic states, promising reduced power consumption and increased recording density. However, integration of magnetoelectric heterostructure into MRAM is a highly challenging task owing to the particular architecture requirements of each component. Here, we show an epitaxial growth of self-assembled $CoFe_2O_4$ nanostripes with bistable in-plane magnetizations on $Pb(Mg,Nb)O_3$—$PbTiO_3$ (PMN—PT) substrates, where the magnetic switching can be triggered by *E*-induced elastic strain effect. An unprecedented magnetic coercive field change of up to 600 Oe was observed with increasing *E*. A near 180° magnetization rotation can be activated by *E* in the vicinity of the magnetic coercive field. These findings might help to solve the 1/2-selection problem in traditional MRAM by providing reduced magnetic coercive field in *E* field selected memory cells.

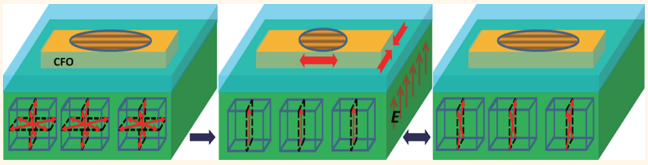

KEYWORDS: magnetoelectric · magnetic anisotropy · magnetoresistance · self-assembled film

Magnetoresistive random-access memory (MRAM) is a nonvolatile recording technology that uses both charge and spin degrees of freedom to encode information.[1] With fast access time and unlimited endurance, MRAM is predicted to be the next generation "universal" memory. However, a low storage density and high writing energy consumption present challenges to the practical application of MRAM.[2] Special considerations have been placed on shape design of the patterned nanomagnets, device architecture design, and magnetization switching mechanism.[3,4] Nanomagnetic elements with a large in-plane aspect ratio are adopted as the free switching layer where two possible stable magnetic domains are antiparallel with each other, producing different resistive states in the magnetic tunnel junction (MTJ). A large shape anisotropy guarantees stability but also hampers the magnetization switching during the writing process. Therefore, a large magnetic force is required to overcome the large energy barrier between the two distinct magnetic states. Extensive research has been done to overcome the anisotropy energy to favor the writing process, including spin-polarized current injection,[5] voltage-induced anisotropy,[6,7] and elastic strain effect.[8]

Magnetoelectric (ME) coupling has been widely recognized as a promising solution to reduce the writing energy and improve the recording density by manipulation of magnetic orders with electric field.[9−14] Although novel single phase ME materials have been widely studied, the largest ME coupling coefficients are reported in bilayer ME heterostructures.[15] The two most promising scenarios for ME-based MRAM are (i) electric field controlled magnetic exchange bias,[16−18] and (ii) electric field induced

* Address correspondence to zgwang@vt.edu.

Received for review February 26, 2014 and accepted August 5, 2014.

Published online August 05, 2014
10.1021/nn503369y

strain effect on magnetic easy axis rotation.[19−21] In the first scenario, an interfacial exchange coupling between multiferroic $BiFeO_3$ and various ferromagnetic thin films has been well studied. However, a magnetic exchange bias field (H_{ex}) larger than the original magnetic coercive field (H_c) is difficult to be induced by electric field; therefore, the remanent magnetization is not a determined value after application of different magnetic fields. Moreover, the low operating temperature of full electric field controlled exchange bias hampers room-temperature applications.[22] In the second scenario, ME effect has been widely investigated in controlling the magnetization state in single-domain magnetic nanostructures.[23,24] Ni nanobars have been deposited on $Pb(Zr,Ti)O_3$ films where the domain state in Ni can be controlled by the external electric field through electromechanical coupling induced strain.[23] Ni nanocrystals on PMN−PT single crystal also show large magnetic coercive field shift under different strain conditions.[24] A strain mediated magnetoelectric random access memory (SME-RAM) has been proposed and predicted to possess ultrahigh recording density and low energy consumption, utilizing strain controlled magnetic easy axis rotation to switch the resistance state in the MTJ for information encoding.[2,25] However, the specific magnetic domain orientation cannot be predicted due to the bistable magnetization states along the field-dependent magnetic easy axis, which can lead to a unpredictable resistance state in the MTJ.[1,2,4]

Here, we report growth of novel self-assembled $CoFe_2O_4$ (CFO) nanostripes on piezoelectric PMN−PT substrate where bistable magnetizations, an important attribute in MRAM free layer, can be established due to a large magnetic shape anisotropy. Electric field modulation of the strain state was utilized to control the magnetic coercive field of the ferromagnetic component. The electric field dependence of magnetization switching promises a simple and practical electric field assisted magnetization switching random-access memory (EAMS-RAM) where information is recorded in an electric field selected cell by a current producing a magnetic field.

Self-assembled $CoFe_2O_4$−$BiFeO_3$ (CFO−BFO) heterostructures grown on piezoelectric 0.71Pb(Mg,Nb-)O_3−0.29$PbTiO_3$ (PMN−PT) single crystals act as a prototype for the verification of the working principle of the proposed EAMS-RAM. There are three reasons why we selected CFO−BFO/PMN−PT: (i) CFO forms in-plane nanostripes with a length/width aspect ratio of $R \approx 4{:}1$ embedded in a BFO matrix when grown on ⟨011⟩ oriented perovskite substrates; thus, the giant magnetic shape anisotropy results in bistable magnetic domain orientations, which makes it a perfect example for the magnetic free layer in MRAM;[26] (ii) ⟨110⟩ oriented PMN−PT can provide a large uniaxial in-plane strain due to an electric field induced phase transition;[13] and (iii) both CFO and BFO have proper crystal lattice mismatch with a PMN−PT substrate, and the epitaxial interface guarantees an effective strain transfer from PMN−PT to CFO component.[21]

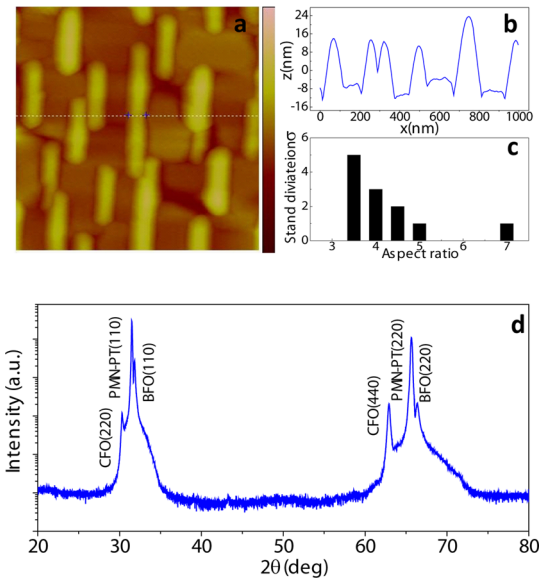

Figure 1. Morphology and magnetic phase distribution in CFO−BFO self-assembled thin films. (a) Topography as seen by AFM, working at tapping mode, showing CFO nanostripes jutting out for ∼20 nm from the BFO matrix; line profile of height (b) and aspect ratio standard deviation (c) of CFO nanostripes; and (d) XRD line scan of the separated BFO and CFO peaks as well as PMN−PT substrate peaks.

RESULTS AND DISCUSSION

Thin films of CFO−BFO with separated CFO and BFO components have been widely reported. Most of them concern CFO−BFO layers grown on ⟨001⟩ oriented substrates, where CFO perpendicular nanopillars are embedded in a BFO matrix.[27,28] However, CFO nanoarrays favor perpendicular magnetic recording, but not MRAM recording, where bistable horizontal magnetizations are needed.[29] Fortunately, it has been found that CFO−BFO forms a different architecture when grown on ⟨011⟩ oriented perovskites: instead of perpendicular nanopillars, CFO elongates along the in-plane ⟨0$\bar{1}$1⟩, forming a flat nanostripe structure, resulting in bistable magnetizations along the in-plane ⟨0$\bar{1}$1⟩.[26] Figure 1 shows the morphology and crystalline characterization of a CFO−BFO film on ⟨011⟩ PMN−PT. BFO formed as the matrix due to an easier wetting with the substrate,[30] whereas CFO nucleated as nanostripes sticking out for ∼25 nm from the BFO matrix, as shown in Figure 1a,b. The widths of the CFO nanostripes were relatively stable (∼68 nm), whereas their lengths varied from 230 to 530 nm. Figure 1c shows the standard deviation of the CFO nanostripe aspect ratios. All CFO nanostripes had an aspect ratio larger than 3:1, and the much longer stripe may have been formed by the merging of the two stripes. An average length/width aspect ratio of $R \approx 4{:}1$ was calculated (Supporting

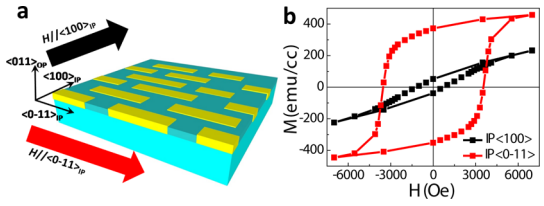

Figure 2. Schematic of the phase architecture of BFO−CFO on a PMN−PT substrate (a) and the M−H loops showing a strong magnetic easy axis along in-plane ⟨0$\bar{1}$1⟩ and a magnetic hard axis along in-plane ⟨100⟩ (b). The in-plane measurement directions of the sample were determined by the XRD measurement and the M−H loops were obtained by VSM at room temperature.

Information Figure S1 and Table S-I). Figure 1d shows the XRD result for a CFO−BFO/PMN−PT heterostructure. Both the CFO and BFO peaks were found to be in accordance with the substrate orientation, demonstrating an epitaxial interface between the CFO−BFO film and PMN−PT substrate.

Figure 2 shows the magnetic hysteresis (M−H) loops along different in-plane directions. The CFO nanostripes were elongated along the in-plane ⟨0$\bar{1}$1⟩, referred to as IP1, with a length/width aspect ratio of $R \approx 4$, as shown in the schematic in Figure 2a. Therefore, a magnetic shape anisotropy induced magnetic easy axis was defined along IP1. The M−H loop shows a large coercive field of $H_{c\text{-}ip1} \approx 3600$ Oe and a large magnetic squareness factor of $R = M_0/M_{7k} \approx 0.8$ along IP1, where M_0 is the remanent magnetization at a magnetic field of $H = 0$ Oe and M_{7k} is the magnetization at $H = 7000$ Oe. The large remanent magnetization means that the magnetization can be retained after removal of external magnetic field: it is thus a nonvolatile memory effect. The large magnetic coercive field promises higher resistivity to environmental thermal fluctuation and a higher recording density.[31−33] In contrast, the in-plane ⟨100⟩, referred to as IP2, was the magnetic hard axis, which exhibited a small $H_{c\text{-}ip2} = 800$ Oe and a small $R = 0.18$. More importantly, the remanent magnetization along IP1 was about ten times larger than that along IP2, indicating that the magnetic domains can only be stabilized along the magnetic easy axis (*i.e.*, IP1).

Magnetic strain and crystalline anisotropy can also influence the magnetic properties in ferromagnetic nanostructures. Our previous investigations have systematically studied the relationship between magnetic strain and shape anisotropies in CFO−BFO self-assembled films, where the magnetic response was dominated by shape anisotropy.[26] Moreover, CFO experienced a compressive strain along the length direction due to a larger lattice parameter compared with the BFO matrix. Therefore, the magnetic strain anisotropy also preferred a magnetic easy axis along IP1. CFO has a large first order magneto-crystalline anisotropy (MCA) constant of $K_1 = 2 \times 10^6$ erg/cm^3. Therefore, the MCA energy difference between the ⟨100⟩ and ⟨0$\bar{1}$1⟩ directions is $\Delta = K_{\langle 100\rangle} - K_{\langle 0\bar{1}1\rangle} = K_0 - [(K_0 - K_1)/4] = 5 \times 10^5$ erg/cm^3,[26] which is close to the shape anisotropy energy of the CFO nanostructure with an aspect ratio $R \approx 4$. MCA prefers a magnetic easy axis along the in-plane ⟨100⟩, which counteracts the magnetic shape anisotropy. However, it has been reported that the effective MCA energy (K_{eff}) is strongly dependent on the size of the magnetic nanostructures.[34,35] Detailed studies of the CFO magnetic crystalline anisotropy have shown a weak MCA compared with the magnetic shape anisotropy for CFO epitaxial thin films on (001) and (011) oriented $SrTiO_3$ substrates (see Supporting Information). In a few words, the magnetic shape anisotropy dominates the magnetic properties in CFO nanostripes, resulting in a strong magnetic easy axis along IP1.

Patterned magnetic units with large aspect ratios are necessary for the stabilization of bistable magnetic domains in the magnetic free layer in MRAM. Therefore, self-assembled CFO nanostripes with two stable in-plane magnetization states can act as an ideal prototype to study the effect of ME interactions on magnetization switching during the MRAM writing process. The ME effect is produced by a coupling of electric dipoles and electron spins, through interfacial elastic strain transferred between ferroelectric and ferromagnetic components. It has been well recognized that non-180° ferroelastic switching, instead of 180° ferroelectric switching, is the critical factor for magnetization manipulation.[36,37] Also, the horizontal interface between the thin film and the substrate determines that only the in-plane elastic strain can be effectively transferred through the heterostructure. The ⟨011⟩ oriented PMN−PT in the vicinity of the morphotropic phase boundary possesses giant transverse piezoelectric coefficients, $d_{31} \approx -2740$ pm/V and $d_{32} \approx 1100$ pm/V,[38] due to the formation of intermediate monoclinic phases where the polarization is no longer constrained along certain crystallographic directions but rather can freely rotate within planes.[39] More interestingly, the phase transformation induced in-plane strain is uniaxial, which is compressive along IP1 and tensile along IP2. Therefore, opposite magnetic property changes can be anticipated along IP1 and IP2, respectively.

Figure 3 shows a schematic of the ME coupling in the CFO−BFO/PMN−PT heterostructure. The giant electromechanical response in PMN−PT single crystals is attributed to, instead of ferroelectric domain motion, the phase instability induced by polar nanoregions with typical correlation distance smaller than 10 nm.[40−43] In the present investigation, the reversible strain is induced by an *E* controlled phase transformation; therefore, modulation of the strain ambient of CFO nanostripes is not constrained by the size of the ferroelectric domains in PMN−PT. Upon application of an electric field *E* along the out-of-plane ⟨011⟩, the

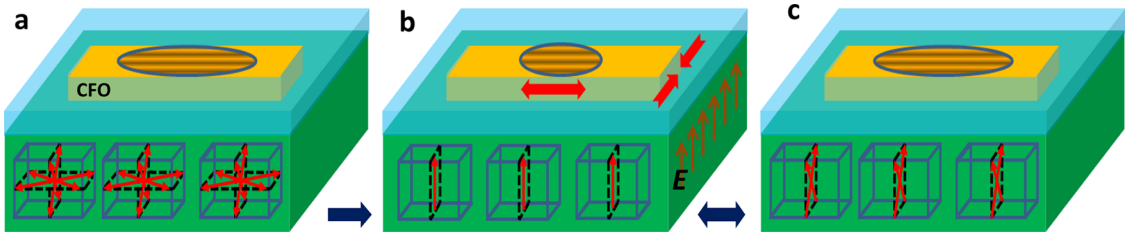

Figure 3. Schematic of the electric field controlled magnetic anisotropy energy distribution in a single CFO nanostripe. (a) Initial state with large magnetic anisotropy energy along IP ⟨0$\bar{1}$1⟩: the length direction of CFO stripe; (b) drastically reduced magnetic anisotropy energy along IP ⟨0$\bar{1}$1⟩ due to electric field induced tensile strain along ⟨0$\bar{1}$1⟩; and (c) recovery of the large magnetic anisotropy energy upon removal of electric field.

polarizations according to R-phase will rotate and align their moments in accordance to *E*, forming a pseudo monodomain O phase, as shown in Figure 3b. After removal of *E*, the monodomain O phase is not stable, and the polarizations deviate from the out-of-plane ⟨011⟩ rotating toward the M_B structure. Therefore, an *E* // ⟨011⟩ can switch the PMN−PT substrate between O and M_B phases, and thus significantly alter the magnetic anisotropy distribution in the CFO nanostripes. Under an out-of-plane *E*, PMN−PT stays in the O phase and the CFO nanostripe experiences compressive and tensile strains along ⟨100⟩ and ⟨0$\bar{1}$1⟩, respectively. CFO has a negative magnetostriction along both ⟨100⟩ and ⟨0$\bar{1}$1⟩. Therefore, the magnetization switching along ⟨0$\bar{1}$1⟩ becomes easier due to tensile strain and that along ⟨100⟩ becomes more difficult due to compressive strain. On the whole, the *E* induced magnetic strain anisotropy competes with magnetic shape anisotropy, reducing the energy barrier between the two stable magnetization directions along the length of the CFO nanostripes. As a consequence, magnetization switching can be modulated by electric field *via* the ME coupling.

Figure 4 shows the electric field dependence of the magnetic properties and crystal lattice parameters. For $E = 0$ kV/cm, the CFO nanostripes had a large remanent magnetization and a large coercive field ($H_c \approx$ 3600 Oe), as shown in Figure 4a. For *E* applied out-of-plane, the M−H loop shrank due to the *E* induced magnetic strain anisotropy. The remanent magnetization decreased from 308 to 270 emu/cc and the magnetization squareness ratio (Sq = M_0/M_{7k}) decreased from Sq ≈ 0.77 to Sq ≈ 0.70. More importantly, the coercive field decreased from 3600 to 3000 Oe, resulting in a giant magnetic coercive field difference of ΔH_c = 600 Oe, which is dramatically larger than the other reported ME heterostructures.[10,11,20,44,45] The change of the H_c value was induced by the magnetic strain anisotropy, which is linear with the elastic strain. Therefore, the value of H_c in CFO is strongly related to the crystal lattice parameter change of the PMN−PT substrate. For *E* applied out-of-plane, a ⟨011⟩ oriented PMN−PT substrate experiences tensile strains along both ⟨011⟩ and ⟨0$\bar{1}$1⟩, whereas the strain along ⟨100⟩ is compressive. Here, we use the out-of-plane ⟨011⟩ strain

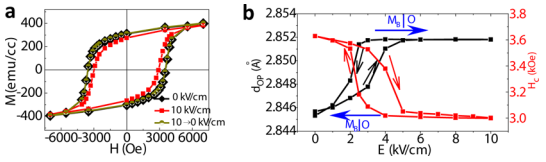

Figure 4. Electric field dependence of H_c and the phase transformation induced large change in crystal lattice parameters in the PMN−PT substrate. (a) Reduction of M−H loops upon application of electric field, where H_c decreased from 3600 to 3000 Oe, and then increased to 3600 Oe after removal of the electric field; and (b) H_c and out-of-plane *d*-spacing value as functions of electric field.

as a estimate of the strain change tendency along the in-plane ⟨0$\bar{1}$1⟩, as both of them are induced by the phase transformation which affects the lattice parameters along all directions simultaneously.[38,46,47] Figure 4b shows the electric field dependence of H_c along ⟨0$\bar{1}$1⟩ and the *d*-spacing along ⟨011⟩ (d_{OP}) at room temperature. With increasing *E* to 5 kV/cm, the value of d_{OP} can be seen to continuously increase from 2.846 to 2.852 Å resulting in a 0.2% elongation. For $E >$ 5 kV/cm, the value of d_{OP} was stable due to the completion of the $M_B \rightarrow$ O phase transformation. With decreasing *E* between 5 and 2.5 kV/cm, the d_{OP} value change revealed hysteresis due to the induced $M_B \rightarrow$ O transformation. For $E <$ 2.5 kV/cm, the O phase did not remain stable, but rather the M_B phase was recovered (Supporting Information Figure S4 and Table S-II). In comparison, the H_c change followed exactly the opposite trend with d_{OP}. The value of H_c decreased from 3600 to 3050 Oe as *E* was increased from 0 to 5 kV/cm, then, it became relatively stable for $5 < E < 10$ kV/cm due to the completed phase transformation. During the decreasing *E* process, a H_c hysteresis loop was also found between $5 > E > 2$ kV/cm (Supporting Information Figure S5).

Next, we show a dynamic analysis of the *E* modulated M in Figure 5. The CFO−BFO/PMN−PT heterostructure was premagnetized at −7000 Oe, and then six different opposite magnetic fields were applied to switch the magnetization. The magnetic coercive field of the CFO nanostructures decreased from $H_{c\text{-}0}$ = 3600 Oe to $H_{c\text{-}E}$ = 3000 Oe after application of $E = 10$ kV/cm, showing a giant magnetic coercive field shift of ΔH_c = 600 Oe. For $-3000 < H < 0$ Oe, the external magnetic

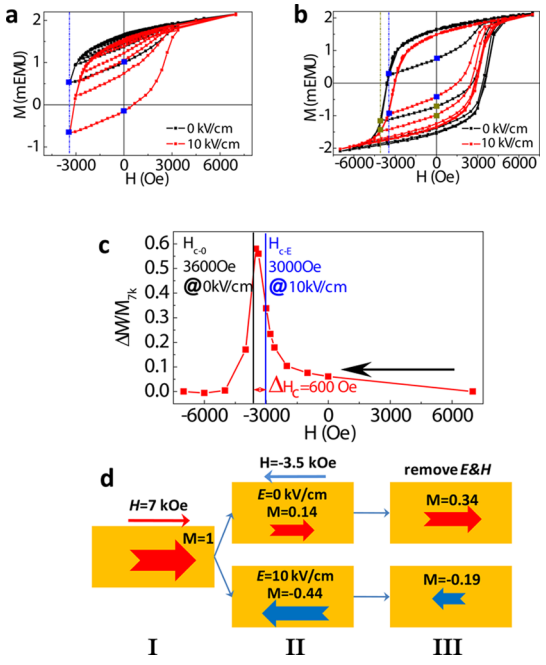

Figure 5. Magnetic response at 0, −1000, −2000, −2600, −2800, −3000, −3380 Oe (a) and −3500, −4000, −5000, −6000 Oe (b) for premagnetized CFO−BFO/PMN−PT under different electric field conditions (Measurement magnetic field *H* was first set to be 7 kOe which slowly decreased to a series of negative magnetic fields and then increased to 7 kOe, showing *E* effect on the magnetization reversal behavior); (c) magnetization difference as a function of switching magnetic field for CFO−BFO/PMN−PT under different electric field conditions; (d) schematic of electric field triggered magnetization switching at −3500 Oe. The magnetization value at 7 kOe was normalized to be 1. Then, a negative magnetic field *H* = −3.5 kOe was applied to switch the magnetic domains in CFO nanostripes. An external electric field *E* = 10 kV/cm was proved to be able to trigger the magnetization reversal at this condition, which could not be realized at zero electric field condition.

field was smaller than the coercive fields for both CFO−BFO/PMN−PT with and without *E*. Therefore, the magnetization stayed in the predefined direction and ΔM was small, as shown in Figure 5a,c. For $-7000 < H < 3600$ Oe, the external magnetic field *H* was larger than the coercive fields for CFO−BFO/PMN−PT with and without *E*. Therefore, the magnetization could be switched for both CFO−BFO/PMN−PT with and without *E*, and thus, ΔM was small, as shown in Figure 5b,c. For $-3600 < H < -3000$ Oe, which is in the electric field assisted magnetization switching region (EAMSR), the magnetization switching in CFO−BFO/PMN−PT could be triggered by electric field. Therefore, a dramatic magnetization difference was observed for the samples with different *E*. The magnetization of the one with *E* can be switched by *H*, whereas the magnetization of that without *E* could not be switched by *H*. This reveals a giant magnetization difference of $\Delta M/M_s > 0.35$ within the whole EAMSR, as shown in Figure 5c. The magnetic field dependence of the magnetization difference is demonstrated in Figure 5c, where a giant $\Delta M/M_s$ of up to 57% was found at $H = -3500$ Oe. Figure 5d shows the

TABLE 1. Magnetization Measurements upon Application of Different Magnetic Fields Inside and Outside of EAMSR

point no.	*H* (Oe)	M_0/M_{7k} @0 kV/cm	M_0/M_{7k} @10 kV/cm	$\Delta M/M_{7k}$
1	+7000	+1.00	+1.00	0
2	−3380	+0.25	−0.31	0.56
3	0	+0.46	−0.06	0.52
4	−3500	+0.14	−0.44	0.58
5	0	+0.34	−0.19	0.53
6	−4000	−0.52	−0.69	0.17
7	0	−0.33	−0.47	0.14

schematic of how to use *E* to trigger the *M* switching in EAMSR. In stage I, CFO nanostripes were magnetized by a large *H* and *M* was normalized to be 1. Then, an opposite magnetic field within EAMSR was applied across the sample in stage II. Two different magnetization switching processes happened based on different *E* values. For *E* = 0 kV/cm, the magnetization could not be switched due to the large H_c, whereas for *E* = 10 kV/cm, the magnetization could be switched due to a decreased H_c induced by the elastic strain mediated ME effect. Moreover, after removal of *E* and *H*, the switched and unswitched magnetizations could be maintained, demonstrating two distinct magnetization states that can be effectively controlled by electric field.

Table 1 shows the magnetization switching condition for different magnetic fields. At $H_1 = 7000$ Oe, all *M*'s were aligned parallel with *H*; therefore, $\Delta M/M_s \approx 0$. At $H_2 = -3380$ and $H_4 = -3500$ Oe, which were within the EAMSR, *M* was switched for *E* = 10 kV/cm but not switched for *E* = 0 kV/cm. Therefore, the magnetization differences were large with $\Delta M/M_s \approx 0.56$ and 0.58 for H_2 and H_4, respectively. Moreover, the magnetization differences were stable after removal of the magnetic field. $\Delta M/M_s \approx 0.52$ and 0.53 were found at H_3 and $H_5 = 0$ Oe after removal of H_2 and H_4, respectively. This shows that the electric field assisted magnetization switching was stable after removal of the external magnetic field. At $H_6 = -4000$ Oe, *M* could be switched regardless of *E*; therefore, the magnetization difference $\Delta M/M_{7k}$ was significantly decreased to 0.17.

Figure 6 shows the electric field dependence of the magnetization under different dc bias magnetic fields (H_b). Before each *M* measurement, the CFO−BFO/PMN−PT was premagnetized by $H = -7000$ Oe. At $H_b = 0$ Oe, *M* was stable in the initial stage. Then, it decreased from −1.5 mEMU to −1.27 mEMU after application of *E* = 10 kV/cm, due to the *E* induced magnetic strain anisotropy. (Here we compare the absolute value of *M* and the signs only to demote the magnetic moment directions.) After removal of *E*, *M* increased to −1.44 mEMU due to a released magnetic strain anisotropy. At $H_b = 1000$ Oe, *M* decreased from −1.24 to −0.97 mEMU for *E* = 10 kV/cm and then increased to −1.15 mEMU. At $H_b = 3300$ Oe, *M* changed its direction, increasing from −0.22 to 1.32 mEMU

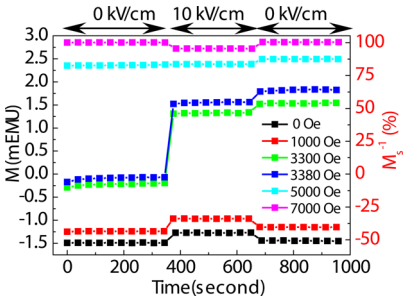

Figure 6. Magnetization measurements at different dc magnetic fields for different electric field conditions. The sample was premagnetized by $H = -7$ kOe before measurement. For $H = 0$, 1 kOe, E can not trigger the magnetization reversal. For $H = 5$, 7 kOe, the magnetization reversal can be realized without application of E. For $H = 3300$, 3380 Oe, the magnetization reversal can be triggered by E, which would retain its original orientation with only H.

under E = 10 kV/cm, due to the electric field assisted magnetization switching. After removal of E, M further increased to 1.54 mEMU. A similar M evolution was found for H_b = 3380 Oe with M increasing with two steps from −0.07 to 1.56 and then to 1.85 mEMU. At H_b = 5000 Oe, M showed no obvious change after application of E. This can be explained by a competition of E assisted M switching and the magnetic strain anisotropy. The former effect preferred a full switching of M, while the latter encouraged magnetic moments to deviate from the easy axis: thus, the final result was a stable M. After removal of E, M then increased due to a release of the magnetic strain anisotropy. At H_b = 7000 Oe, M was fully switched and therefore only a magnetic strain anisotropy effect was observed: M decreased from 2.85 to 2.70 mEMU upon application of E, and then recovered its original value after removal of E. The electric field induced magnetic strain anisotropy was reversible in the selected PMN−PT substrate, and thus the strain induced ΔM was small and volatile which is not practical for memory application. On the other hand, a dramatic magnetization difference was obtained in the EAMSR due to the E induced 180° magnetization switching. More importantly, this magnetization switching induced ΔM was nonvolatile, promising memory functions.

All of the above results are statistical averaged values over all CFO nanostripes. In CFO−BFO self-assembled structures, the aspect ratios of the CFO nanostripes are not entirely uniform; therefore, the magnetic coercive field and EAMSR for each CFO nanostripe was different. This explains the not so large Barkhausen jump near the magnetic coercive field and a 60% (but not 100%) magnetization switching induced by electric field within EAMSR, as shown in Figure 6.

CONCLUSIONS

In summary, we have demonstrated an electric field assisted magnetization switching in CFO−BFO/PMN−PT heterostructures, where a unique strong in-plane magnetic easy axis in CFO stripes and a uniaxial ferroelastic strain in PMN−PT substrates are coupled to each other *via* interface elastic strain. An unprecedented large magnetic coercive field shift of 600 Oe was induced by electric field, based on which a new design of MRAM with an electric field addressed writing process was proposed. The preliminary results of CFO−BFO/PMN−PT prototype revealed the effectiveness of electro-mechanical-magnetic coupling and provided more freedom for design of magnetization based memories. Furthermore, strain modulation of magnetization is a long-range effect in contrast with short-range interface effects, *i.e.*, interface superconductivity[48] and magnetic exchange bias;[14] therefore, the unprecedented board magnetic coercive field tunability reported here holds great promise for novel spintronics and microwave devices where considerable film thickness is required for functionality.[49−53]

EXPERIMENTAL METHODS

Film Growth. CFO−BFO self-assembled nanostructures were prepared by pulsed laser deposition, using a 248 nm KrF laser and a composite target of composition 65 atom % BFO and 35 atom % CFO. The (011) oriented PMN-29PT substrates were used for the growth of CFO−BFO with different phase architectures. Growth was carried out at 700 °C in an oxygen atmosphere (100 mTorr) with a laser energy density of ~3 J/cm^2 at 10 Hz. The distance between the target and substrates was 6 cm. An epitaxial film thickness of ~400 nm was obtained after 1 h deposition.

Characterization of Structure and Properties. The crystal lattice and thin film orientation were analyzed by a Philips X'pert high-resolution X-ray diffractometer with a X-ray wavelength of Cu Kα = 1.5406 Å designed for single-crystalline samples. The film topography was studied by a Veeco SPI 3100 working in a AFM mode. Magnetic hysteresis loops were measured using a Lakeshore 7300 series vibrating sample magnetometer (VSM) system at room temperature. Before magnetic property measurements, 30 nm Au electrodes were sputtered on both top and bottom side of CFO−BFO/PMN−PT heterostructure using a SPI module sputter coater. The sample was fixed on the VSM holder with silver paste which also acted as the conducting channel to the outside dc power supply. Melted wax was also used in the edge of the sample for further fixation; otherwise, the large in-plane strain would detach the sample from the VSM holder.

Conflict of Interest: The authors declare no competing financial interest.

Acknowledgment. This work was supported by Air Force Office of Scientific Research (FA9550-09-1-0552) in USA.

Supporting Information Available: Additional data on morphology measurement by atomic force microscopy and $CoFe_2O_4$ (CFO) nanostripe aspect ratio calculation, comparison of magnetic shape and crystalline anisotropy, XRD line scans of electric field dependence of crystal lattice parameters, and electric field dependence of M−H loops of CFO−BFO/PMN−PT. This material is available free of charge *via* the Internet at http://pubs.acs.org.

REFERENCES AND NOTES

1. Akerman, J. Toward a Universal Memory. *Science* **2005**, *308*, 508–510.
2. Hu, J.-M.; Li, Z.; Chen, L.-Q.; Nan, C.-W. High-Density Magnetoresistive Random Access Memory Operating at Ultralow Voltage at Room Temperature. *Nat. Commun.* **2011**, *2*, 553.
3. Zheng, Y. F.; Zhu, J. G. Switching Field Variation in Patterned Submicron Magnetic Film Elements. *J. Appl. Phys.* **1997**, *81*, 5471–5473.
4. Zhu, J. G.; Zheng, Y. F.; Prinz, G. A. Ultrahigh Density Vertical Magnetoresistive Random Access Memory. *J. Appl. Phys.* **2000**, *87*, 6668–6673.
5. Albert, F. J.; Katine, J. A.; Buhrman, R. A.; Ralph, D. C. Spin-Polarized Current Switching of a Co Thin Film Nanomagnet. *Appl. Phys. Lett.* **2000**, *77*, 3809–3811.
6. Wang, W. G.; Li, M. G.; Hageman, S.; Chien, C. L. Electric-Field-Assisted Switching in Magnetic Tunnel Junctions. *Nat. Mater.* **2012**, *11*, 64–68.
7. Nozaki, T.; Shiota, Y.; Shiraishi, M.; Shinjo, T.; Suzuki, Y. Voltage-Induced Perpendicular Magnetic Anisotropy Change in Magnetic Tunnel Junctions. *Appl. Phys. Lett.* **2010**, *96*, 022506.
8. Eerenstein, W.; Mathur, N. D.; Scott, J. F. Multiferroic and Magnetoelectric Materials. *Nature* **2006**, *442*, 759–765.
9. Sahoo, S.; Polisetty, S.; Duan, C. G.; Jaswal, S. S.; Tsymbal, E. Y.; Binek, C. Ferroelectric Control of Magnetism in $BaTiO_3$/Fe Heterostructures *via* Interface Strain Coupling. *Phys. Rev. B* **2007**, *76*, 092108.
10. Gepraegs, S.; Brandlmaier, A.; Opel, M.; Gross, R.; Goennenwein, S. T. B. Electric Field Controlled Manipulation of the Magnetization in Ni/$BaTiO_3$ Hybrid Structures. *Appl. Phys. Lett.* **2010**, *96*, 142509.
11. Liu, M.; Obi, O.; Cai, Z.; Lou, J.; Yang, G.; Ziemer, K. S.; Sun, N. X. Electrical Tuning of Magnetism in Fe_3O_4/PZN-PT Multiferroic Heterostructures Derived by Reactive Magnetron Sputtering. *J. Appl. Phys.* **2010**, *107*, 073916.
12. Wu, T.; Bur, A.; Wong, K.; Hockel, J. L.; Hsu, C.-J.; Kim, H. K. D.; Wang, K. L.; Carman, G. P. Electric-Poling-Induced Magnetic Anisotropy and Electric-Field-Induced Magnetization Reorientation in Magnetoelectric Ni/(011) $[Pb(Mg_{1/3}Nb_{2/3})O_3]_{(1-x)}$-$[PbTiO_3]_x$ Heterostructure. *J. Appl. Phys.* **2011**, *109*, 07D732.
13. Wang, Z.; Wang, Y.; Ge, W.; Li, J.; Viehland, D. Volatile and Nonvolatile Magnetic Easy-Axis Rotation in Epitaxial Ferromagnetic Thin Films on Ferroelectric Single Crystal Substrates. *Appl. Phys. Lett.* **2013**, *103*, 132909.
14. Park, J. H.; Lee, J.-H.; Kim, M. G.; Jeong, Y. K.; Oak, M.-A.; Jang, H. M.; Choi, H. J.; Scott, J. F. In-Plane Strain Control of the Magnetic Remanence and Cation-Charge Redistribution in $CoFe_2O_4$ Thin Film Grown on a Piezoelectric Substrate. *Phys. Rev. B* **2010**, *81*, 134401.
15. Zhai, J.; Xing, Z.; Dong, S.; Li, J.; Viehland, D. Magnetoelectric Laminate Composites: An Overview. *J. Am. Ceram. Soc.* **2008**, *91*, 351–358.
16. Bibes, M.; Barthelemy, A. Multiferroics: Towards a Magnetoelectric Memory. *Nat. Mater.* **2008**, *7*, 425–426.
17. Chu, Y.-H.; Martin, L. W.; Holcomb, M. B.; Gajek, M.; Han, S.-J.; He, Q.; Balke, N.; Yang, C.-H.; Lee, D.; Hu, W.; *et al.* Electric-Field Control of Local Ferromagnetism Using a Magnetoelectric Multiferroic. *Nat. Mater.* **2008**, *7*, 478–482.
18. Zhao, T.; Scholl, A.; Zavaliche, F.; Lee, K.; Barry, M.; Doran, A.; Cruz, M. P.; Chu, Y. H.; Ederer, C.; Spaldin, N. A.; *et al.* Electrical Control of Antiferromagnetic Domains in Multiferroic $Bifeo_3$ Films at Room Temperature. *Nat. Mater.* **2006**, *5*, 823–829.
19. Eerenstein, W.; Wiora, M.; Prieto, J. L.; Scott, J. F.; Mathur, N. D. Giant Sharp and Persistent Converse Magnetoelectric Effects in Multiferroic Epitaxial Heterostructures. *Nat. Mater.* **2007**, *6*, 348–351.
20. Weiler, M.; Brandlmaier, A.; Gepraegs, S.; Althammer, M.; Opel, M.; Bihler, C.; Huebl, H.; Brandt, M. S.; Gross, R.; Goennenwein, S. T. B. Voltage Controlled Inversion of Magnetic Anisotropy in a Ferromagnetic Thin Film at Room Temperature. *New J. Phys.* **2009**, *11*, 013021.
21. Wang, Z.; Yang, Y.; Viswan, R.; Li, J.; Viehland, D. Giant Electric Field Controlled Magnetic Anisotropy in Epitaxial $Bifeo_3$-$Cofe_2o_4$ Thin Film Heterostructures on Single Crystal $Pb(Mg_{1/3}Nb_{2/3})_{0.7}Ti_{0.3}O_3$ Substrate. *Appl. Phys. Lett.* **2011**, *99*, 043110.
22. Wu, S. M.; Cybart, S. A.; Yi, D.; Parker, J. M.; Ramesh, R.; Dynes, R. C. Full Electric Control of Exchange Bias. *Phys. Rev. Lett.* **2013**, *110*, 067202.
23. Chung, T.-K.; Keller, S.; Carman, G. P. Electric-Field-Induced Reversible Magnetic Single-Domain Evolution in a Magnetoelectric Thin Film. *Appl. Phys. Lett.* **2009**, *94*, 132501.
24. Kim, H. K. D.; Schelhas, L. T.; Keller, S.; Hockel, J. L.; Tolbert, S. H.; Carman, G. P. Magnetoelectric Control of Superparamagnetism. *Nano Lett.* **2013**, *13*, 884–888.
25. Hu, J.-M.; Nan, C. W. Electric-Field-Induced Magnetic Easy-Axis Reorientation in Ferromagnetic/Ferroelectric Layered Heterostructures. *Phys. Rev. B* **2009**, *80*, 224416.
26. Wang, Z.; Li, Y.; Viswan, R.; Hu, B.; Harris, V. G.; Li, J.; Viehland, D. Engineered Magnetic Shape Anisotropy in $BiFeO_3$-$CoFe_2O_4$ Self-Assembled Thin Films. *ACS Nano* **2013**, *7*, 3447–3456.
27. Zheng, H.; Straub, F.; Zhan, Q.; Yang, P.-L.; Hsieh, W.-K.; Zavaliche, F.; Chu, Y.-H.; Dahmen, U.; Ramesh, R. Self-Assembled Growth of $BiFeO_3$-$CoFe_2O_4$ Nanostructures. *Adv. Mater.* **2006**, *18*, 2747–2752.
28. Zheng, H.; Zhan, Q.; Zavaliche, F.; Sherburne, M.; Straub, F.; Cruz, M. P.; Chen, L.-Q.; Dahmen, U.; Ramesh, R. Controlling Self-Assembled Perovskite-Spinel Nanostructures. *Nano Lett.* **2006**, *6*, 1401–1407.
29. Zavaliche, F.; Zhao, T.; Zheng, H.; Straub, F.; Cruz, M. P.; Yang, P. L.; Hao, D.; Ramesh, R. Electrically Assisted Magnetic Recording in Multiferroic Nanostructures. *Nano Lett.* **2007**, *7*, 1586–1590.
30. Yan, L.; Yang, Y.; Wang, Z.; Xing, Z.; Li, J.; Viehland, D. Review of Magnetoelectric Perovskite-Spinel Self-Assembled Nano-Composite Thin Films. *J. Mater. Sci.* **2009**, *44*, 5080–5094.
31. Challener, W. A.; Peng, C.; Itagi, A. V.; Karns, D.; Peng, W.; Peng, Y.; Yang, X.; Zhu, X.; Gokemeijer, N. J.; Hsia, Y. T.; *et al.* Heat-Assisted Magnetic Recording by a near-Field Transducer with Efficient Optical Energy Transfer. *Nat. Photonics* **2009**, *3*, 220–224.
32. Kryder, M. H.; Gage, E. C.; McDaniel, T. W.; Challener, W. A.; Rottmayer, R. E.; Ju, G.; Hsia, Y.-T.; Erden, M. F. Heat Assisted Magnetic Recording. *Proc. IEEE* **2008**, *96*, 1810–1835.
33. Zhu, L.; Nie, S.; Meng, K.; Pan, D.; Zhao, J.; Zheng, H. Multifunctional $L1_0$-$Mn_{1.5}Ga$ Films with Ultrahigh Coercivity, Giant Perpendicular Magnetocrystalline Anisotropy and Large Magnetic Energy Product. *Adv. Mater.* **2012**, *24*, 4547–4551.
34. Herzer, G. Grain-Size Dependence of Coercivity and Permeability in Nanocrystaline Ferromagnets. *IEEE Trans. Magn.* **1990**, *26*, 1397–1402.
35. LesliePelecky, D. L.; Rieke, R. D. Magnetic Properties of Nanostructured Materials. *Chem. Mater.* **1996**, *8*, 1770–1783.
36. Baek, S. H.; Jang, H. W.; Folkman, C. M.; Li, Y. L.; Winchester, B.; Zhang, J. X.; He, Q.; Chu, Y. H.; Nelson, C. T.; Rzchowski, M. S.; *et al.* Ferroelastic Switching for Nanoscale Non-Volatile Magnetoelectric Devices. *Nat. Mater.* **2010**, *9*, 309–314.
37. Balke, N.; Choudhury, S.; Jesse, S.; Huijben, M.; Chu, Y. H.; Baddorf, A. P.; Chen, L. Q.; Ramesh, R.; Kalinin, S. V. Deterministic Control of Ferroelastic Switching in Multiferroic Materials. *Nat. Nanotechnol.* **2009**, *4*, 868–875.
38. Lu, Y.; Jeong, D. Y.; Cheng, Z. Y.; Zhang, Q. M.; Luo, H. S.; Yin, Z. W.; Viehland, D. Phase Transitional Behavior and Piezoelectric Properties of the Orthorhombic Phase of $Pb(Mg_{1/3}Nb_{2/3})O_3$-$PbTiO_3$ Single Crystals. *Appl. Phys. Lett.* **2001**, *78*, 3109–3111.
39. Fu, H. X.; Cohen, R. E. Polarization Rotation Mechanism for Ultrahigh Electromechanical Response in Single-Crystal Piezoelectrics. *Nature* **2000**, *403*, 281–283.
40. Xu, G.; Shirane, G.; Copley, J. R. D.; Gehring, P. M. Neutron Elastic Diffuse Scattering Study of $Pb(Mg_{1/3}Nb_{2/3})O_3$. *Phys. Rev. B* **2004**, *69*, 064112.

41. Xu, G.; Wen, J.; Stock, C.; Gehring, P. M. Phase Instability Induced by Polar Nanoregions in a Relaxor Ferroelectric System. *Nat. Mater.* **2008**, *7*, 562–566.
42. Xu, G.; Zhong, Z.; Hiraka, H.; Shirane, G. Three-Dimensional Mapping of Diffuse Scattering in $Pb(Zn_{1/3}Nb_{2/3})O_3$-$xPbTiO_3$. *Phys. Rev. B* **2004**, *70*, 174109.
43. Xu, G. Y.; Zhong, Z.; Bing, Y.; Ye, Z. G.; Shirane, G. Electric-Field-Induced Redistribution of Polar Nano-Regions in a Relaxor Ferroelectric. *Nat. Mater.* **2006**, *5*, 134–140.
44. Wang, J.; Ma, J.; Li, Z.; Shen, Y.; Lin, Y.; Nan, C. W. Switchable Voltage Control of the Magnetic Coercive Field *via* Magnetoelectric Effect. *J. Appl. Phys.* **2011**, *110*, 043919.
45. Liu, M.; Obi, O.; Lou, J.; Li, S.; Xing, X.; Yang, G.; Sun, N. X. Tunable Magnetoresistance Devices Based on Multiferroic Heterostructures. *J. Appl. Phys.* **2011**, *109*, 07D913.
46. Renault, A. E.; Dammak, H.; Calvarin, G.; Gaucher, P.; Thi, M. P. Electric-Field-Induced Orthorhombic Phase in $Pb[(Zn_{1/3}Nb_{2/3})_{0.955}Ti_{0.045}]O_3$ Single Crystals. *J. Appl. Phys.* **2005**, *97*, 044105.
47. Cao, H.; Bai, F.; Wang, N.; Li, J.; Viehland, D.; Xu, G.; Shirane, G. Intermediate Ferroelectric Orthorhombic and Monoclinic M_b Phases in [110] Electric-Field-Cooled $Pb(Mg_{1/3}Nb_{2/3})$-O_3−30%$PbTiO_3$ Crystals. *Phys. Rev. B* **2005**, *72*, 064104.
48. Reyren, N.; Thiel, S.; Caviglia, A. D.; Kourkoutis, L. F.; Hammerl, G.; Richter, C.; Schneider, C. W.; Kopp, T.; Ruetschi, A. S.; Jaccard, D.; *et al.* Superconducting Interfaces between Insulating Oxides. *Science* **2007**, *317*, 1196–1199.
49. Sun, N. X.; Srinivasan, G. Voltage Control of Magnetism in Multiferroic Heterostructures and Devices. *SPIN* **2012**, *02*, 1240004.
50. Das, J.; Song, Y.-Y.; Mo, N.; Krivosik, P.; Patton, C. E. Electric-Field-Tunable Low Loss Multiferroic Ferrimagnetic-Ferroelectric Heterostructures. *Adv. Mater.* **2009**, *21*, 2045–2049.
51. Harris, V. G.; Geiler, A.; Chen, Y.; Yoon, S. D.; Wu, M.; Yang, A.; Chen, Z.; He, P.; Parimi, P. V.; Zuo, X.; *et al.* Recent Advances in Processing and Applications of Microwave Ferrites. *J. Magn. Magn. Mater.* **2009**, *321*, 2035–2047.
52. Jalli, J.; Hong, Y.-K.; Bae, S.; Lee, J.-J.; Abo, G. S.; Lyle, A.; Gee, S.-H.; Lee, H.; Mewes, T.; Sur, J.-C.; *et al.* Growth and Characterization of 144 μM Thick Barium Ferrite Single Crystalline Film for Microwave Device Application. *J. Appl. Phys.* **2009**, *105*, 07A511.
53. Kranov, Y. A.; Abuzir, A.; Prakash, T.; McIlroy, D. N.; Yeh, W. J. Barium Hexaferrite Thick Films Made by Liquid Phase Epitaxy Reflow Method. *IEEE Trans. Magn.* **2006**, *42*, 3338–3340.